# Metal phosphides embedded with in situ-formed metal phosphate impurities as buffer materials for high-performance potassium-ion batteries

*Shunping Ji, Chunyan Song, Junfeng Li, Kwan San Hui*, Wenjun Deng, Shuo Wang, Haifeng Li, Duc Anh Dinh, Xi Fan, Shuxing Wu, Jintao Zhang, Fuming Chen, Zongping Shao*, and Kwun Nam Hui**

S. P Ji, J. F. Li, S. Wang, Prof. H. F. Li, Prof. K. N. Hui
Joint Key Laboratory of the Ministry of Education, Institute of Applied Physics and Materials Engineering, University of Macau, Avenida da Universidade, Taipa, Macau SAR, P.R. China
E-mail: bizhui@um.edu.mo

C. Y. Song
Analysis and Testing Center, Shenzhen Technology University, Shenzhen 518118, China

Prof. K. S. Hui
School of Engineering, Faculty of Science, University of East Anglia, Norwich, NR4 7TJ, United Kingdom
E-mail: k.hui@uea.ac.uk

W. J. Deng
School of Advanced Materials, Peking University Shenzhen Graduate School, Shenzhen 518055, China

Prof. D. A. Dinh
NTT hi-tech insitute, Nguyen Tat Thanh university, Ho Chi Minh city 700000, Vietnam

Prof. X. Fan
Ningbo Institute of Materials Technology, Engineering, Chinese Academy of Sciences, Ningbo, 315201, P.R. China

Prof. S. X. Wu
School of Chemical Engineering and Light Industry, Guangdong University of Technology, Guangzhou 510006, PR China

Prof. J. T. Zhang
Key Laboratory for Colloid and Interface Chemistry, Ministry of Education, School of Chemistry and Chemical Engineering, Shandong University, Jinan 250100, China

Prof. F. M. Chen
State Key Laboratory of Optic Information Physics and Technologies, School of Physics and Telecommunication Engineering, South China Normal University, Guangzhou, China 510006, China

Prof. Z. P. Shao
WA School of Mines: Minerals, Energy and Chemical Engineering (WASM-MECE), Curtin University, Perth, WA 6845, Australia
E-mail: zongping.shao@curtin.edu.au

**Keywords:** metal phosphide anode, amorphous phosphates, buffer volume expansion, SEI, PIBs

As anodes for metal-ion batteries, metal phosphides usually suffer from severe capacity degradation because of their huge volume expansion and unstable solid electrolyte interphase (SEI), especially for potassium-ion batteries (PIBs). To address these issues, this study proposes amorphous phosphates acting as buffer materials. Ten types of metal phosphide composites embedded with in situ-formed amorphous phosphates are prepared by one-step ball milling using red phosphorus and corresponding metal oxides as starting materials. Zinc phosphide composite is selected for further study as a PIB anode. Benefitting from the effective suppression of volume variation, a KF-rich SEI is formed on the electrode surface in the KFSI-based electrolyte. The zinc phosphide composite exhibits a high reversible specific capacity and outstanding long-term cycling stability (476 mA h $g^{-1}$ over 350 cycles at 0.1 A $g^{-1}$ after going through a rate capability test and 177 mA h $g^{-1}$ after 6,000 cycles at 1.0 A $g^{-1}$) and thus achieves the best cycling performance among all reported metal phosphide-based anodes for PIBs. This study highlights a low-cost and effective strategy to guide the development of metal phosphides as high-performance anodes for PIBs.

## 1. Introduction

Potassium-ion batteries (PIBs) show great promise for next-generation energy storage devices owing to the high natural abundance of potassium (K) (≈1,400 times the abundance of lithium), their potential high energy density, and their low cost.[1] The standard hydrogen potential of $K/K^+$ (−2.93 V vs. SHE) is close to that of lithium-ion batteries (LIBs, −3.04 V vs. SHE) and lower than that of sodium-ion batteries (SIBs, −2.70 V vs. SHE). Notably, the potential of PIBs is even lower than that of LIBs in propylene carbonate electrolytes.[2] Furthermore, $K^+$ ions are expected to have a fast ion diffusion rate in electrolytes due to their Stokes radii in water and other organic solvents being lower than those of $Li^+$ and $Na^+$ as a

result of their weak coulombic interactions with solvent molecules.[1b, 3] Such advantages endow PIBs with high-voltage operation and high-power density.

Various types of anodes and cathodes have been investigated for use in PIBs. Among the reported PIB anodes, such as carbon-based materials,[4] metals (e.g., Bi,[5] and Sb[6]), and chalcogenides (e.g., $Sb_2S_3$,[7] $MoS_{1.5}Se_{0.5}$,[8] and $MoSe_2$[9]), phosphorus and metal phosphides have relatively high theoretical specific capacity, reasonable voltage platform, and low cost.[10] However, these materials usually undergo fast capacity decay during cycling because of significant volume changes.[11] For example, the volume expansion rate of phosphorus for a PIB anode can be as high as 300%.[10c] Huge volume variations not only result in the pulverization of active materials and exfoliation from current collectors but also affect the formation of a stable solid electrolyte interphase (SEI).[12]

Many strategies have been employed to suppress the volume expansion of electrodes for PIBs. In particular, morphology engineering is one of the most commonly used approaches and involves nano-sized particles,[13] core–shell structures,[14] nanofibers[10d, 15], etc. In addition, using flexible substrates[16] and high-concentration electrolytes[17] has shown positive effects on the alleviation of volume expansion. However, complicated morphology control technology and high-cost additives are not favorable for practical applications. The inactive components in electrodes, including the binders, separators, collectors, and conductive agents, can also function as buffer materials.[18] Some in situ-formed inactive components (CaO and $MgF_2$) in electrode materials show an excellent capability of buffering volume variations on the basis of the "spectator effect."[19] Despite the high purity of starting materials and the inert atmosphere during preparation, the introduction of phosphorus oxides or phosphate impurities has been found to be inevitable for phosphorus- and metal phosphide-based electrodes due to the oxidation during the exposure of electrode materials to air.[14b, 20] Research has indicated that the presence of P–O bonds in electrode materials enhances the electrochemical properties, which contribute to the formation of a stable SEI or even an increase in capacity.[21] In particular,

phosphate groups ($PO_4^{3-}$), as polyanions, have widely been designed as electrode materials,[22] ion conductors,[21c, 23] and even corrosion-resistant coatings[24] because of their excellent structural and electrochemical stability. In addition, metal phosphates easily form glassy states (amorphous states).[25] Several studies have demonstrated that amorphous materials have shown better capability of buffering volume variations than their crystalline states and that they exhibit relatively high capacity and ion diffusion rate when used as electrode materials.[26] For example, an in situ-formed amorphous $Na_4P_2O_7$ embedded Sn presents a high specific capacity (480 mA h $g^{-1}$at 50 mA $g^{-1}$) and excellent cycling stability (over 70% retained after 15,000 cycles) as an SIB anode.[27] Therefore, incorporating amorphous phosphates as buffer materials can be expected to reduce volume expansion and enhance the cycling stability of metal phosphides.

Inspired by these facts, we directly utilize metal oxides (MOs) and red phosphorus (RP) as starting materials to prepare metal phosphides with in situ-formed metal phosphates by using the ball milling method. Ten types of metal phosphides are successfully prepared using this method. In this work, we focus on zinc phosphide as a representative PIB anode to verify our strategy. ZnO is ball milled with RP and Super P to prepare a zinc phosphide composite with amorphous zinc phosphate ZnO@P(1:2)@C, to which carbon (Super P) is added to enhance the electrical conductivity of zinc phosphide. To confirm the role of amorphous zinc phosphate on the cycling stability of zinc phosphide, we also ball mill Zn metal with RP and Super P in the preparation of zinc phosphide without zinc phosphate, Zn@P(1:2)@C. Different from Zn@P(1:2)@C, the ZnO@P(1:2)@C sample displays an entirely amorphous structure under the same preparation conditions. As expected, amorphous phosphates help relieve the volume expansion of the metal phosphide, leading to the formation of a stable KF-rich SEI in 1.0 M KFSI (EC/DEC, v/v = 1:1) electrolyte. A PIB assembled with the ZnO@P(1:2)@C electrode exhibits excellent cycle stability with a reversible discharge capacity of 177 mA h $g^{-1}$ after 6,000 cycles at 1.0 A $g^{-1}$.

## 2. Results and discussion

Deviating from the routine preparation of metal phosphides, we chose MOs instead of high-purity metal powder as raw materials to obtain metal phosphide composites embedded with in situ-formed metal phosphates by using a high-energy ball milling (HEBM) process. As shown in **Scheme 1**, 10 types of metal phosphides ($VP_x$, $CrP_x$, $MnP_x$, FeP, $FeP_2$, $FeP_4$, CoP, $NiP_3$, $CuP_2$, and $ZnP_2$) embedded with amorphous metal phosphates were successfully obtained using the corresponding MOs and RP as raw materials. Figure S1 (Supporting Information, SI) shows the XRD data of these metal phosphides. No obvious diffraction peaks belonging to the metal phosphates were observed in all the metal phosphides that were prepared by using MOs. However, we did confirm the presence of metal phosphates by Fourier transform infrared spectroscopy (FTIR) (Figure S2, SI). Obvious asymmetric stretch peaks of the metal phosphates at 700–1,300 $cm^{-1}$ were detected in all the obtained metal phosphide composites. This result proved the effectiveness of a simple and universal method for preparing metal phosphides embedded with uniform amorphous phosphates. In the subsequent work, zinc phosphide is selected for further analysis to confirm the findings due to its huge volume expansion (404%) and high theoretical capacity (842 mA h $g^{-1}$) as a PIB anode by theoretical calculation.[28] The performance of other phosphides will be presented in our future work.

Zinc phosphide composites prepared by controlling different mole ratios of ZnO and RP were investigated and labeled as ZnO@P(mole ratio). For ZnO@P(4:1) and ZnO@P(2:1) samples, Zn metal particles (JCPDS no. 87-0713) and unreacted ZnO (JCPDS no. 76-0704) were detected because of the lack of RP (Figure S3a, SI). In addition, $Zn_3P_2$ (JCPDS no. 74-1156) was observed in the ZnO@P(2:1) sample. When the molar ratio of RP to ZnO was over 1.0, the $ZnP_2$-dominated phase was obtained (Figure S3b, SI). For the ZnO@P(1:2) sample, a similar $ZnP_2$ product (JCPDS no. 72-1626 and JCPDS no. 44-1237) was formed, but this sample was unstable when exposed to air because some excess RP was converted to white phosphorus (WP)

(Figure S4a and S4b, SI).[29] The excess P for the ZnO@P(1:2) sample was analyzed using a thermal gravimetric analyzer (TGA) (Figure S5, SI). The experimental content of the excess P (10.5 %) was slightly lower than the theoretical value (10.8%) because of the formation of WP, which had been removed by $CS_2$ before testing. By contrast, ZnO@P(2:3) (**Figure 1**a) displayed the purest $ZnP_2$ phase (α-$ZnP_2$, JCPDS no. 72-1626) and the highest diffraction peak intensity among all the ZnO@P compounds prepared. $ZnP_2$ belonged to the tetragonal phase, and the space group was $P4_12_12$. The corresponding SEM, TEM, SAED pattern, and HRTEM images of ZnO@P(2:3) were shown in Figure S6, SI. The lattice parameters (a = b = 5.0748 Å, c = 18.5551 Å, $R_{wp}$ = 5.94%, $\chi^2$ = 2.55) were similar to those reported for $ZnP_2$[30] and those of the Zn@P(1:2)@C sample prepared by Zn metal (**Figure 1**b, a = b = 5.0748 Å, c = 18.5601 Å, $R_{wp}$ = 7.89%, $\chi^2$ = 1.29). **Figure 1**c shows the XRD pattern for ZnO@P(1:2)@C showing the amorphous phase after  The crystal structure of $ZnP_2$ with tetragonal phase and $P4_12_12$ space group is shown in **Figure 1**d, and the complete details of the Rietveld refinement data are shown in Table S1 and S2. No diffraction peaks belonging to phosphates were observed for all the ZnO@P samples owing to the amorphous structure. The composition of the ZnO@P(2:3) sample was also detected by TGA (Figure S7a, SI). The experimental mass fractions of $ZnP_2$ and $Zn_3(PO_4)_2$ were 65.3wt% and 34.7wt%, which are close to the theoretical values of 62.3wt% and 37.7wt%, respectively.

In sum, the proposed mole ratio of ZnO to RP for the synthesis of the $ZnP_2$ composite is as follows:

$8ZnO + 12P \rightarrow 5ZnP_2 + Zn_3(PO_4)_2$ ($3ZnO{\cdot}P_2O_5$, amorphous)

After the addition of Super P (30wt%), the ZnO@P(1:2)@C (Figure S8, SI) and ZnO@P(2:3)@C (Figure S9, SI) samples exhibited amorphous states (Figure 1c and S3c, SI). Different from ZnO@P(1:2), the amorphous ZnO@P(1:2)@C sample showed good environmental stability when exposed to air because the excessive RP was stabilized by carbon to form stable P–C bonds and avoid the formation of WP.[31] In addition, the amorphous

ZnO@P(1:2)@C sample exhibited good structural stability, and its amorphous state was maintained even after heating to 400 °C for 2 h in $N_2$ atmosphere (Figure S4c, d, SI), although excessive P was evaporated and partially converted to WP (Figure S4e, f, SI) under this condition. These results further confirmed the surplus of P in the ZnO@P(1:2) sample. The crystalline $Zn_3(PO_4)_2$ (JCPDS No. 76-05180) phase was detected when heating ZnO@P(1:2)@C to 800 °C for 2 h owing to the melting and recrystallization of the amorphous zinc phosphate (Figure S4c, SI). Crystalline $ZnP_2$ was also detected after reducing the carbon content of ZnO@P(1:2)@C to 10wt% (Figure S3d, SI), thus suggesting the generation of $ZnP_2$. The crystalline Zn@P(1:2)@C sample was also transformed into the amorphous state by directly adding 30wt% zinc phosphate (Figure S3d, SI). The coexistence of zinc phosphate and carbon seemed conducive to the formation of amorphous zinc phosphide, its mechanism will be analyzed in our future work.

**Figure 1**e shows the high-resolution TEM image of ZnO@P(1:2)@C, in which no lattice fringes belonging to $ZnP_2$ and zinc phosphate were observed, except the (002) plane of Super P with a d-spacing of 0.352 nm.[32] The selected area electron diffraction pattern also confirmed the amorphous nature of ZnO@P(1:2)@C with several dark diffraction rings rather than diffraction spots (**Figure 1**f), and this result is in accordance with the XRD data. Energy dispersive X-ray spectroscopy (EDS) mappings indicated the homogeneous distribution of P, O, C, and Zn in ZnO@P@C (**Figure 1**h–k). By contrast, obvious lattice fringes belonging to $ZnP_2$ were observed in Zn@P(1:2)@C (Figure S10, SI) and ZnO@P(2:3), and they revealed the polycrystalline states of the samples. This result is consistent with those of the XRD. No lattice fringes belonging to zinc phosphate were found in the Zn@P(1:2)@C and ZnO@P(2:3) samples.

**Figure 2**a also provides the infrared spectra to confirm the existence of phosphates. Relative to Zn@P(1:2)@C, ZnO@P(1:2)@C and ZnO@P(2:3) showed distinct vibration peaks belonging to the $(PO_4)^{3-}$ group located at 1,000 $cm^{-1}$, but no obvious vibration peak splitting

occurred for $Zn_3(PO_4)_2$ because of its amorphous structure.[33] Super P carbon was also verified by Raman spectroscopy. Two peaks at 1,340 and 1,586 $cm^{-1}$ in **Figure 2**b for Zn@P(1:2)@C and ZnO@P(1:2)@C demonstrated the disordered (D) band and graphitic (G) band of the added carbon, respectively.[34] High-resolution XPS spectra revealed the bonding information of the three samples. The C 1s spectra displayed obvious C=C/C-C ($sp^2$, 284.6 eV) and C-C ($sp^3$, 285.4 eV) peaks belonging to Super P for the ZnO@P(1:2)@C and Zn@P(1:2)@C samples (**Figure 2**c). A P–C (283.8 eV) bond was also detected; such bond is easily formed during HEBM and contributes to the electrical conductivity of materials.[31] The P–C bond for the ZnO@P(1:2)@C sample was also confirmed by Raman spectroscopy (Figure S11, SI). Relative to ZnO@P(1:2), ZnO@P(1:2)@C showed a weak broad peak in the range of 600–700 $cm^{-1}$, which was ascribed to the P–C bond.[31, 35] The P 2p spectra showed Zn–P/P–P ($2p_{3/2}$, 129.8 eV) and Zn–P/P–P ($2p_{1/2}$, 130.9 eV) peaks in the three samples, indicating the formation of zinc phosphide. Strong P–O–P/P–$O^-$ (133.5 eV) peaks belonging to phosphates were detected for ZnO@P(1:2)@C and ZnO@P(2:3).[36] By contrast, a weak P–O–P/P–$O^-$ peak was observed for Zn@P(1:2)@C due to the inevitable oxidation of metal phosphides when the samples were exposed to air. The O 1s spectra were fitted into the C–O/P–$O^-$ (531.9 eV) and C=O/P–O–P (533.5 eV) bonds in accordance with the C 1s and P 2p spectra. Furthermore, Zn $2p_{3/2}$ (1,022.2 eV) and Zn $2p_{1/2}$ (1,045.3 eV) revealed the existence of Zn element in the three samples. The Nitrogen adsorption–desorption isotherms and pore size distribution of ZnO@P(1:2)@C, Zn@P(1:2)@C and ZnO@P(2:3) were also provided in Figure S12.

K-ion half-cell tests were conducted to verify the validity of our approach. Amorphous phosphates can decrease volume variations and enhance SEI and cyclic stability. Two types of electrolytes were used: 0.8 M $KPF_6$ and 1.0 M KFSI in EC/DEC (v/v = 1/1). These electrolytes were chosen because KFSI-based electrolytes can form a more stable SEI than the electrolytes based on $KPF_6$ on the surface of K metal and anode materials.[5b, 37] **Figure 3**a shows the cyclic voltammetry (CV) curves of the first five cycles of ZnO@P(1:2)@C in the KFSI electrolyte at

a scan rate of 0.05 mV $s^{-1}$ in the voltage window of 0.01–3.0 V. The first cycle showed maximum cathodic peaks starting from 0.58 V because of the potassiation reaction of the anode and side reaction to form the SEI.[38] From the second cycle, the charge–discharge curves tended to be stable. The cathodic and anodic reactions started from 1.0 and 0.5 V, respectively. Relative to the CV curves of Zn@P(1:2)@C, those of the ZnO@P(1:2)@C electrode reflected a distinct cathodic peak in 0.5 V as a result of the contribution of excess P (Figure S13, SI). The CV curves of ZnO@P(1:2)@C and Zn@P(1:2)@C electrodes at various scan rates in KFSI electrolyte and their corresponding linear relationship between *log (i)* vs *log (v)* showed inevitable capacitive potassium ions storage, which can also contribute to some extra capacity (Figure S14, SI). For the battery performance (**Figure 3**b), ZnO@P(1:2)@C showed better rate capability than Zn@P(1:2)@C, especially in the KFSI electrolyte, which delivered reversible capacities of 503.2, 430.3, 405.5, 349.1, 305.0, and 257.0 mA h $g^{-1}$ at current densities of 0.05, 0.1, 0.2, 0.5, 1.0, and 2.0 A $g^{-1}$, respectively. The Galvanostatic intermittent titration technique (GITT) was used to investigate the K-ion diffusion coefficient of ZnO@P(1:2)@C and Zn@P(1:2)@C electrodes. Before the GITT tests, 5 cycles (0.05 A $g^{-1}$) of charge/discharge process were carried out to activate the batteries (Figure S15, SI). Galvanostatic intermittent titration technique tests confirmed that the K-ion diffusion coefficient of ZnO@P(1:2)@C ($0.74–4.17 \times 10^{-11}$ $cm^2$ $s^{-1}$) (Figure S16-17, SI) was an order of magnitude higher than that of Zn@P(1:2)@C ($0.10–2.73\times10^{-12}$ $cm^2$ $s^{-1}$) (Figure S18-19, SI) during discharging in the KFSI electrolyte because of its amorphous structure, which is more conducive to improving the utilization rate of $ZnP_2$. When reverting the current density to 0.1 A $g^{-1}$ after the rate capability test, the ZnO@P(1:2)@C electrode retained a high reversible capacity and good cyclic stability (476 mA h $g^{-1}$ at the 350th cycle) in the KFSI electrolyte. By contrast, Zn@P(1:2)@C only retained a discharge capacity of 135.7 mA h $g^{-1}$ after 350 cycles. The calculation of specific capacity for the ZnO@P(1:2)@C and Zn@P(1:2)@C electrodes was based on the weights of all the ingredients, except Super P, which had low specific capacity. The rate performance and

cycling performance of Super P in 0.8 M $KPF_6$ and 1.0 M KFSI electrolytes were shown in Figure S20 (SI). **Figure 3**c provides the corresponding galvanostatic charge/discharge profiles of ZnO@P(1:2)@C at the current densities of 0.05–2.0 A $g^{-1}$ in the KFSI electrolyte; these profiles are similar to those of the reported $ZnP_2$ as an SIB anode.[30a] In addition, the extremely small differences in the charge/discharge profiles at the 100th, 200th, and 300th cycles suggested the good electrochemical stability of the ZnO@P(1:2)@C electrode (**Figure 3**d). Different capacity decay processes were clearly observed for the ZnO@P(1:2)@C and Zn@P(1:2)@C electrodes in the two electrolytes at 0.5 A $g^{-1}$ (**Figure 3**e). In the $KPF_6$ electrolyte, the Zn@P(1:2)@C sample obviously suffered from severe capacity degradation, and its reversible capacity was only 70.7 mA h $g^{-1}$ after 250 cycles. As for ZnO@P(1:2)@C, its reversible capacity was 279.8 mA h $g^{-1}$ at the 250th cycle. For ZnO@P(1:2)@C, accelerated capacity fading occurred after about 250 cycles because of the consumption of the $KPF_6$ electrolyte (details will be given later). The ZnO@P(1:2)@C and Zn@P(1:2)@C electrodes showed better cycling stability in the KFSI electrolyte than in the $KPF_6$ electrolyte owing to the formation of a stable SEI.[5b, 37a] After 200 cycles, Zn@P(1:2)@C underwent fast capacity degradation similar to that in the $KPF_6$ electrolyte. Meanwhile, ZnO@P(1:2)@C maintained a reversible capacity of 330 mA h $g^{-1}$ after 500 cycles with a capacity retention rate of 94% (calculated based on the 5th and 500th cycles).[17a] To further demonstrate the superior stability of the prepared samples, we conducted a longer cycling stability test at 1.0 A $g^{-1}$ in the KFSI electrolyte (**Figure 3**f). The retained specific discharge capacity of Zn@P(1:2)@C was only 65 mA h $g^{-1}$ after 1,000 cycles; however, for ZnO@P(1:2)@C, the retained capacity was 177 mA h $g^{-1}$ after 6,000 cycles with a capacity fading rate of 0.0077% per cycle (calculated for the 5th and 6,000th cycles); such capacity is comparable to those of reported metal phosphides and other advanced PIB anodes (**Figure 3**g and Table S3). Furthermore, ZnO@P(1:2)@C also showed high specific capacity and good cycling stability when used as LIB and SIB anodes (Figure S21, SI). To confirm the universality and validity of our strategy for improving the

cycling performance of metal phosphides, we also tested the electrochemical properties of FeP and $NiP_3$ respectively prepared by $Fe_2O_3$ and NiO for PIB anodes (Figure S22 and S23, SI). The results showed the good cycling stability of FeP and $NiP_3$ prepared by $Fe_2O_3$ and NiO, respectively.

Although the battery tests proved the effectiveness of our design, we performed further analysis to support our results. First, the effect of inhibiting the volume expansion for ZnO@P(1:2)@C was verified by disassembling the batteries after 500 cycles (0.5 A $g^{-1}$). For the Zn@P(1:2)@C electrode, the optical images showed the depletion of electrolytes and the falling off of the active materials from the current collectors in the two electrolytes (Figure S28a, b, SI). Moreover, a large number of huge cracks and cavities were observed on the electrode surface by SEM (**Figure 4**a, b), indicating the huge volume variation of the Zn@P(1:2)@C electrode. As for the ZnO@P(1:2)@C electrodes, although the $KPF_6$-based electrolyte was also exhausted, hence explains the accelerated capacity decay after 250 cycles at 0.5 A $g^{-1}$, the active materials were still tightly bound to the current collector (Figure S24c, SI). In the KFSI electrolyte, no active materials fell off, and the electrolyte was not exhausted for the ZnO@P(1:2)@C electrode (Figure S24d, SI). Furthermore, no obvious cracks and voids were found for the ZnO@P(1:2)@C electrode in the two electrolytes (**Figure 4**c, d). Such results verified the electrode's good ability to inhibit volume expansion. In addition, we compared the thickness changes of the ZnO@P(1:2)@C and Zn@P(1:2)@C electrodes before and after potassiation in the KFSI electrolyte. As shown in **Figure 4**e, after discharging to 0.01 V, the thickness (h) of the Zn@P(1:2)@C electrode increased from the original 34 μm to 75 μm (0.01 V) while that of the ZnO@P(1:2)@C electrode changed from 44 μm to 72 μm (0.01 V). If the change of the electrode area was ignored, the volume change rates ($\Delta V = (h_{0.01V} - h_{original})/h_{original}$) of the Zn@P(1:2)@C and ZnO@P(1:2)@C electrodes were 120.6% and 63.6%, respectively. These results similarly revealed the good ability of ZnO@P(1:2)@C to inhibit volume expansion. Second, to elucidate the positive role of amorphous phosphate in relieving volume

variation and enhancing cycling stability, we directly added different mass fractions (10wt% and 20wt%) of zinc phosphate to the Zn@P(1:2)@C sample. The XRD patterns showed that the crystalline $ZnP_2$ phase (JCPDS no. 72-1626) was maintained and that the added zinc phosphate powder was converted to an amorphous state after mixing by ball milling (600 rpm, 6 h) (Figure S25a, SI). For the Zn@P(1:2)@C sample with 20wt% zinc phosphate, its cycling stability obviously improved, and it delivered a discharge capacity of 359.5 mA h $g^{-1}$ after 400 cycles at 0.1 A $g^{-1}$ in the KFSI electrolyte (where the added zinc phosphate served as the active material) (Figure S25b, SI). Notably, huge cracks were observed on the surface of Zn@P(1:2)@C electrode with 10wt% $Zn_3(PO_4)_2$ after 200 cycles at 0.1 A $g^{-1}$ (Figure S25c, SI), whereas no cracks were observed on the surface of Zn@P(1:2)@C electrode with 20wt% $Zn_3(PO_4)_2$ after 400 cycles (0.1 A $g^{-1}$) by SEM (Figure S25d, SI). This result confirmed the effectiveness of phosphates in enhancing cycling stability and capacity retention by reducing the volume variation. In this work, the electrochemical activity of the crystalline zinc phosphate (Figures S26, SI) and amorphous zinc phosphate (Figures S27, SI) for PIBs was also tested by CV and battery performance. No obvious redox peaks were noted in the CV curves, and the negligible reversible capacity indicated the electrochemical inactivity for the K ion (Figures S28 and S29, SI). To verify the formation of a stable SEI in the KFSI-based electrolyte, we conducted an etching XPS analysis and then compared the differences of the SEIs in the two electrolytes after 500 cycles (0.5 A $g^{-1}$) for the ZnO@P(1:2)@C electrode. **Figure 4**f and g show that the high-resolution XPS spectra of F1s varied with etching time in the KFSI and $KPF_6$ electrolytes. The K–F bond (684.5 eV) was obviously detected in the KFSI-based electrolyte, and the area percentage of the K–F peak almost reached 100% after etching for 1,500 s (Figure 4h); this result indicated the formation of a KF-rich SEI, which contributed to the improved cycling performance.[5b, 37b] By contrast, in the $KPF_6$ electrolyte, dominant C–F and P–F peaks were observed. The C–F (15.1%) and P–F (57.8%) peaks still existed after 1 h etching (**Figure 4**i). The etching XPS spectra of survey, C, O, K elements for ZnO@P(1:2)@C

in 1.0 M KFSI electrolyte after 500 cycles at 0.5 A $g^{-1}$ was shown in Figure S30. This result suggested that a large amount of electrolyte was decomposed, thus leading to the exhaustion of electrolyte and the poor cyclic stability in the $KPF_6$ electrolyte.[37a]

In/ex situ XRD and ex situ TEM were employed to preliminarily disclose the electrochemical reaction mechanism of the discharge (potassiation) and charge (depotassiation) processes for ZnO@P(1:2)@C and Zn@P(1:2)@C in the KFSI electrolyte. We collected XRD data at the different charge and discharge voltages of the first two cycles, as shown in **Figure 5**. For ZnO@P(1:2)@C, the whole potassiation and depotassiation processes were in amorphous states (**Figure 5**b). Even after 350 cycles (0.1 A $g^{-1}$), the electrode still retained an amorphous state when charged to 3.0 V (Figure S31, SI). This result proved the good reversibility of the amorphous structure. When the amorphous electrode discharging to 0.01 V was exposed to air for more than 7 min, diffraction peaks belonging to ZnO (JCPDS No. 76-0704) were detected and were attributed to the oxidization of Zn generated by the potassiation process (Figure S32a, SI). After the exposure of the ZnO@P(1:2)@C electrodes to air for 2 days (Figure S32b, SI), various crystalline by-products were observed as a result of the redox reaction of some unstable discharge products, such as Zn, $K_xO$, and $K_xP$ species. An exception was the electrodes charged to 3.0 V, which still retained the amorphous state because the electrode materials completely reverted to their stable initial states. For Zn@P(1:2)@C (**Figure 5**c), the diffraction peaks of the (104), (112), and (114) planes belonging to $ZnP_2$ decreased (increased) with the potassiation (depotassiation) process, thereby revealing the reversible electrochemical conversion of $ZnP_2$. Similarly, no obvious intermediate phases were detected, except for the Zn metal (JCPDS No. 87-0713) (Figure S32d, SI). The possible reason is that the intermediate phases had poor crystallinity or were unstable and could not be detected. Similar to the ZnO@P(1:2)@C electrode, the electrode discharging to 0.01V was exposed to air for 7 min, and the generated Zn metal was also oxidized to ZnO (Figure S32a, SI). To illustrate whether the generated Zn metal would further react with K to form a $KZn_{13}$ alloy phase, we

directly used a thin Zn plate as the electrode to assemble a Zn–K battery with K metal; for comparison, the same Zn–Li battery was assembled because of its known alloy reaction with Li.[39] The results showed that Zn and Li formed an alloy reaction at a discharge voltage platform of 0.2 V (Figure S33, SI). However, under the same discharge conditions, no prominent voltage platform belonging to the $KZn_x$ alloy reaction was observed for the Zn–K battery. This result suggested that the main potassiation product of $ZnP_2$ was Zn metal, which differed from previous calculation results.[28] To eliminate the effect of ex situ XRD test on the mesophases, we also used in situ XRD in exploring the mesophases of the Zn@P(1:2)@C electrode because of its crystalline structure. **Figure 5**d–g and Figure S32c show the diffraction peak intensities of (104), (112), (114), (212), and (216) ascribed to $ZnP_2$ decreasing (increasing) with the potassiation (depotassiation) process. However, similar to the ex situ XRD results, no obvious intermediate phases or $K_{(3-x)}P$ phases were found, and such outcome suggested poor crystallinity or small crystalline size.[10b, 21d] Therefore, ex situ TEM was also employed to analyze the $K_{(3-x)}P$ phases. As shown in **Figure 5**h–k, the (200) and (202) planes respectively belonging to KP (JCPDS No. 71-1844) and $K_3P$ (JCPDS No. 74-0128) were observed for the Zn@P(1:2)@C electrode discharging to 0.01 V, such conversion phases are the common discharging products for phosphorus and metal phosphides as PIB anodes.[10c, 10d, 40] In sum, the proposed main reactions of potassiation and depotassiation for $ZnP_2$ are as follows:

Potassiation:

$$ZnP_2 + (6-2x)K^+ + (6-2x)e^- \rightarrow Zn + 2K_{(3-x)}P \ (x = 0 \text{ or } 2)$$

Depotassiation:

$$Zn + 2K_{(3-x)}P \rightarrow ZnP_2 + (6-2x)K^+ + (6-2x)e^- \ (x = 0 \text{ or } 2)$$

Based on the conversion-type reaction mechanism, the theoretical capacity of $ZnP_2$ can be as high as 1262 mA h $g^{-1}$ when all P converting to $K_3P$ phase. Therefore, for ZnO@P(1:2)@C electrode, its theoretical capacity reaches up to 686 mA h $g^{-1}$ after considering ZnP2 (55.5wt%) and excess phosphorus (10.8wt%), which explains the high reversible capacity of

ZnO@P(1:2)@C. The rate comparison of the ZnO@P(1:2)@C anode with reported metal phosphides in PIBs was also provided for comparsion (Figure S34, SI).

Full cells were also assembled to verify the feasibility of the processes to practical applications. A Prussian blue analogue (PBA, $K_2FeFe(CN)_6$) and ZnO@P(1:2)@C were used as the cathode and anode, respectively (**Figure 6**a). $K_2FeFe(CN)_6$ was synthesized according to the literature[41], and its electrochemical performance is shown in Figure S35. The The full cells were tested in the voltage range of 0.5–3.8 V in the 1.0 M KFSI electrolyte. The capacity was calculated on the basis of the total active materials of the anode and cathode. **Figure 6**b shows the rate performance of the full cell. The average capacities were 83.9, 76.5, 70.6, and 64.2 mA h $g^{-1}$ at the current densities of 10, 20, 50, and 100 mA $g^{-1}$, respectively. **Figure 6**c shows long-term cycling stability and retained capacity of 49 mA h $g^{-1}$ at 100 mA $g^{-1}$ after 1,200 cycles, thereby proving the stability of ZnO@P(1:2)@C. An energy-saving lamp (1.5 W) and red LEDs can be lighted up by a coin-type full cell, which thus shows potential in practical applications (**Figure 6**d).

## 3. Conclusion

A variety of metal phosphides embedded with amorphous phosphates were successfully obtained by directly using MOs and RP as starting materials in a ball milling method. Zinc phosphide was chosen as a representative material for further research. The introduction of phosphates facilitated the amorphization of zinc phosphide. The amorphous structure of the phosphates and zinc phosphide reduced the volume expansion effectively. A stable KF-rich SEI formed in the 1.0 M KFSI electrolyte, and the long-term cycle stability of zinc phosphide was finally achieved. ZnO@P(1:2)@C presented a reversible capacity of 177 mA h $g^{-1}$ after 6,000 cycles at 1.0 A $g^{-1}$, and the capacity fading rate was only 0.0077% per cycle. Obviously, this low-cost and effective strategy can also be applied to other electrode materials on the basis of

alloying or conversion mechanisms. The results of this work are expected to accelerate the research and application of PIBs.

**Supporting Information**
Supporting Information is available from the Wiley Online Library or from the author.

**Acknowledgements**
This work was funded by the Science and Technology Development Fund, Macau SAR (File no. 0191/2017/A3, 0041/2019/A1, 0046/2019/AFJ, 0021/2019/AIR), University of Macau (File no. MYRG2017-00216-FST and MYRG2018-00192-IAPME) and the UEA funding.

Received: ((will be filled in by the editorial staff))
Revised: ((will be filled in by the editorial staff))
Published online: ((will be filled in by the editorial staff))

**References**

[1] a) M. Li, J. Lu, X. Ji, Y. Li, Y. Shao, Z. Chen, C. Zhong, K. Amine, *Nat. Rev. Mater.* **2020**, 5, 276; b) T. Hosaka, K. Kubota, A. S. Hameed, S. Komaba, *Chem. Rev.* **2020**, 120, 6358.
[2] S. Komaba, T. Hasegawa, M. Dahbi, K. Kubota, *Electrochem. Commun.* **2015**, 60, 172.
[3] F. Sagane, T. Abe, Y. Iriyama, Z. Ogumi, *J. Power Sources* **2005**, 146, 749.
[4] a) W. Zhang, Z. Cao, W. Wang, E. Alhajji, A. H. Emwas, P. Costa, L. Cavallo, H. N. Alshareef, *Angew. Chem. Int. Ed.* **2020**, 59, 4448; b) Z. Jian, W. Luo, X. Ji, *J. Am. Chem. Soc.* **2015**, 137, 11566; c) W. X. Yang, J. H. Zhou, S. Wang, Z. C. Wang, F. Lv, W. S. Zhang, W. Y. Zhang, Q. Sun, S. J. Guo, *Acs Energy Lett.* **2020**, 5, 1653; d) J. Ding, H. Zhang, H. Zhou, J. Feng, X. Zheng, C. Zhong, E. Paek, W. Hu, D. Mitlin, *Adv. Mater.* **2019**, 31, e1900429.
[5] a) J. Huang, X. Lin, H. Tan, B. Zhang, *Adv. Energy Mater.* **2018**, 8, 1703496; b) Q. Zhang, J. Mao, W. K. Pang, T. Zheng, V. Sencadas, Y. Chen, Y. Liu, Z. Guo, *Adv. Energy Mater.* **2018**, 8, 1703288.
[6] J. Zheng, Y. Yang, X. Fan, G. Ji, X. Ji, H. Wang, S. Hou, M. R. Zachariah, C. Wang, *Energy Environ. Sci.* **2019**, 12, 615.
[7] Y. Liu, Z. Tai, J. Zhang, W. K. Pang, Q. Zhang, H. Feng, K. Konstantinov, Z. Guo, H. K. Liu, *Nat. Commun.* **2018**, 9, 1.
[8] H. N. Fan, X. Y. Wang, H. B. Yu, Q. F. Gu, S. L. Chen, Z. Liu, X. H. Chen, W. B. Luo, H. K. Liu, *Adv. Energy Mater.* **2020**, 10, 1904162.
[9] J. Ge, L. Fan, J. Wang, Q. Zhang, Z. Liu, E. Zhang, Q. Liu, X. Yu, B. Lu, *Adv. Energy Mater.* **2018**, 8, 1801477.
[10] a) W. C. Chang, J. H. Wu, K. T. Chen, H. Y. Tuan, *Adv. Sci.* **2019**, 6, 1801354; b) Y. Wu, H. B. Huang, Y. Feng, Z. S. Wu, Y. Yu, *Adv. Mater.* **2019**, 31, 1901414; c) H. Jin, H. Wang, Z. Qi, D. S. Bin, T. Zhang, Y. Wan, J. Chen, C. Chuang, Y. R. Lu, T. S. Chan, H. Ju, A. M. Cao, W. Yan, X. Wu, H. Ji, L. J. Wan, *Angew. Chem. Int. Ed.* **2020**, 59, 2318; d) W. Zhang, W. K. Pang, V. Sencadas, Z. Guo, *Joule* **2018**, 2, 1534.
[11] a) R. Verma, P. N. Didwal, H.-S. Ki, G. Cao, C.-J. Park, *ACS Appl. Mater. Interfaces*

**2019**, 11, 26976; b) W. Zhang, J. Mao, S. Li, Z. Chen, Z. Guo, *J. Am. Chem. Soc.* **2017**, 139, 3316.

[12] J. Chen, X. Fan, Q. Li, H. Yang, M. R. Khoshi, Y. Xu, S. Hwang, L. Chen, X. Ji, C. Yang, H. He, C. Wang, E. Garfunkel, D. Su, O. Borodin, C. Wang, *Nat. Energy* **2020**, 5, 386.

[13] a) P. Xiong, P. Bai, S. Tu, M. Cheng, J. Zhang, J. Sun, Y. Xu, *Small* **2018**, 14, 1802140; b) D. Das, D. Sarkar, S. Nagarajan, D. Mitlin, *Chem. Commun.* **2020**, 56, 14889; c) D. Zhou, J. Yi, X. Zhao, J. Yang, H. Lu, L.-Z. Fan, *Chem. Eng. J.* **2021**, 413, 127508; d) J. Bai, B. Xi, H. Mao, Y. Lin, X. Ma, J. Feng, S. Xiong, *Adv. Mater.* **2018**, 30, 1802310.

[14] a) Q. Tan, W. Zhao, K. Han, P. Li, W. Wang, D. He, Z. Liu, Q. Yu, M. Qin, X. Qu, *J. Mater. Chem. A* **2019**, 7, 15673; b) F. Yang, H. Gao, J. Hao, S. Zhang, P. Li, Y. Liu, J. Chen, Z. Guo, *Adv. Funct. Mater.* **2019**, 29, 1808291.

[15] Y. Liu, Z. Sun, X. Sun, Y. Lin, K. Tan, J. Sun, L. Liang, L. Hou, C. Yuan, *Angew. Chem. Int. Ed.* **2020**, 59, 2473.

[16] a) J. Wang, B. Wang, B. Lu, *Adv. Energy Mater.* **2020**, 10, 2000884; b) X. Zhao, W. Wang, Z. Hou, G. Wei, Y. Yu, J. Zhang, Z. Quan, *Chem. Eng. J.* **2019**, 370, 677; c) R. Zhao, H. Di, X. Hui, D. Zhao, R. Wang, C. Wang, L. Yin, *Energy Environ. Sci.* **2020**, 13, 246.

[17] a) F. Yang, J. Hao, J. Long, S. Liu, T. Zheng, W. Lie, J. Chen, Z. Guo, *Adv. Energy Mater.* **2020**, 11, 2003346; b) J. Xie, Y. Zhu, N. Zhuang, X. Li, X. Yuan, J. Li, G. Hong, W. Mai, *J. Mater. Chem. A* **2019**, 7, 19332.

[18] a) E. Foreman, W. Zakri, M. H. Sanatimoghaddam, A. Modjtahedi, S. Pathak, A. G. Kashkooli, N. G. Garafolo, S. Farhad, *Adv Sustain Syst* **2017**, 1, 1700061; b) F. Jeschull, J. Maibach, *Electrochem. Commun.* **2020**, 121, 106874.

[19] a) O. Ruiz, M. Cochrane, M. Li, Y. Yan, K. Ma, J. Fu, Z. Wang, S. H. Tolbert, V. B. Shenoy, E. Detsi, *Adv. Energy Mater.* **2018**, 8, 1801781; b) X. Xu, C. Niu, M. Duan, X. Wang, L. Huang, J. Wang, L. Pu, W. Ren, C. Shi, J. Meng, B. Song, L. Mai, *Nat. Commun.* **2017**, 8, 460; c) S. Zhou, Z. Tao, J. Liu, X. Wang, T. Mei, X. Wang, *ACS Omega* **2019**, 4, 6452.

[20] a) L. Ran, I. Gentle, T. Lin, B. Luo, N. Mo, M. Rana, M. Li, L. Wang, R. Knibbe, *J. Power Sources* **2020**, 461, 228116; b) Y. Wu, S. Hu, R. Xu, J. Wang, Z. Peng, Q. Zhang, Y. Yu, *Nano Lett.* **2019**, 19, 1351; c) Z. Yan, Z. Huang, H. Zhou, X. Yang, S. Li, W. Zhang, F. Wang, Y. Kuang, *J. Energy Chem.* **2021**, 54, 571; d) W. Li, B. Yan, H. Fan, C. Zhang, H. Xu, X. Cheng, Z. Li, G. Jia, S. An, X. Qiu, *ACS Appl. Mater. Interfaces* **2019**, 11, 22364; e) Y. Yi, W. Zhao, Z. Zeng, C. Wei, C. Lu, Y. Shao, W. Guo, S. Dou, J. Sun, *Small* **2020**, 16, e1906566.

[21] a) H. Tao, S. Du, F. Zhang, L. Xiong, Y. Zhang, H. Ma, X. Yang, *ACS Appl. Mater. Interfaces* **2018**, 10, 34245; b) Y. Qian, S. Jiang, Y. Li, Z. Yi, J. Zhou, T. Li, Y. Han, Y. Wang, J. Tian, N. Lin, Y. Qian, *Adv. Energy Mater.* **2019**, 9, 1901676; c) T. Deng, X. Ji, Y. Zhao, L. Cao, S. Li, S. Hwang, C. Luo, P. Wang, H. Jia, X. Fan, X. Lu, D. Su, X. Sun, C. Wang, J. G. Zhang, *Adv. Mater.* **2020**, 32, 2000030; d) C. Zhao, H. X. Chen, H. D. Liu, L. Yin, Q. B. Zhang, S. C. Yu, P. Liu, G. M. Zhong, C. Z. Lu, Y. Yang, *J. Mater. Chem. A* **2021**, 9, 6274.

[22] a) T. Jin, H. Li, K. Zhu, P. F. Wang, P. Liu, L. Jiao, *Chem. Soc. Rev.* **2020**, 49, 2342; b) C. Masquelier, L. Croguennec, *Chem. Rev.* **2013**, 113, 6552.

[23] a) A. Heller, *Anal. Bioanal. Chem.* **2006**, 385, 469; b) W. Shin, J. Lee, Y. Kim, H. Steinfink, A. Heller, *J. Am. Chem. Soc.* **2005**, 127, 14590.

[24] a) Q. Huang, L. Liu, Z. Wu, S. Ji, H. Wu, P. Chen, Z. Ma, Z. Wu, R. K. Y. Fu, H. Lin, X. Tian, F. Pan, P. K. Chu, *Surf. Coat. Technol.* **2020**, 384, 125321; b) M. Zubielewicz, W. Gnot, *Prog. Org. Coat.* **2004**, 49, 358.

[25] a) M. Maslyk, S. Bach, W. Li, S. I. Shylin, M. Panthöfer, B. Barton, V. Ksenofontov, K.

Xu, B. Meermann, U. Kolb, J. Schmedt auf der Günne, W. Tremel, *J. Phys. Chem. C* **2021**, 125, 2636; b) V. Mathew, S. Kim, J. Kang, J. Gim, J. Song, J. P. Baboo, W. Park, D. Ahn, J. Han, L. Gu, Y. Wang, Y.-S. Hu, Y.-K. Sun, J. Kim, *NPG Asia Mater.* **2014**, 6, e138; c) S. Somrani, C. Rey, M. Jemal, *J. Mater. Chem.* **2003**, 13, 888.

[26] a) L. Fan, X. Li, B. Yan, X. Li, D. Xiong, D. Li, H. Xu, X. Zhang, X. Sun, *Appl. Energy* **2016**, 175, 529; b) X. Niu, Y. Zhang, L. Tan, Z. Yang, J. Yang, T. Liu, L. Zeng, Y. Zhu, L. Guo, *Energy Storage Mater.* **2019**, 22, 160; c) S. Yan, K. P. Abhilash, L. Tang, M. Yang, Y. Ma, Q. Xia, Q. Guo, H. Xia, *Small* **2019**, 15, 1804371; d) D. Li, J. Zhou, X. Chen, H. Song, *ACS Appl. Mater. Interfaces* **2016**, 8, 30899; e) Y. Kim, Y. Park, A. Choi, N. S. Choi, J. Kim, J. Lee, J. H. Ryu, S. M. Oh, K. T. Lee, *Adv. Mater.* **2013**, 25, 3045.

[27] X. Yang, R.-Y. Zhang, J. Zhao, Z.-X. Wei, D.-X. Wang, X.-F. Bie, Y. Gao, J. Wang, F. Du, G. Chen, *Adv. Energy Mater.* **2018**, 8, 1701827.

[28] S. Yu, S. O. Kim, H. S. Kim, W. Choi, *Int. J. Energy Res.* **2019**, 43, 7646.

[29] J. Zhou, X. Liu, L. Zhu, S. Niu, J. Cai, X. Zheng, J. Ye, Y. Lin, L. Zheng, Z. Zhu, D. Sun, Z. Lu, Y. Zang, Y. Wu, J. Xiao, Q. Liu, Y. Zhu, G. Wang, Y. Qian, *Chem* **2020**, 6, 221.

[30] a) K. H. Nam, Y. Hwa, C. M. Park, *ACS Appl. Mater. Interfaces* **2020**, 12, 15053; b) J. G. White, *Acta Cryst.* **1965**, 18, 217.

[31] J. Sun, G. Zheng, H. W. Lee, N. Liu, H. Wang, H. Yao, W. Yang, Y. Cui, *Nano Lett.* **2014**, 14, 4573.

[32] a) C.-M. Wu, P.-I. Pan, Y.-W. Cheng, C.-P. Liu, C.-C. Chang, M. Avdeev, S.-k. Lin, *J. Power Sources* **2017**, 340, 14; b) Z. Tai, Q. Zhang, Y. Liu, H. Liu, S. Dou, *Carbon* **2017**, 123, 54.

[33] a) S. Bach, V. R. Celinski, M. Dietzsch, M. Panthofer, R. Bienert, F. Emmerling, J. Schmedt auf der Gunne, W. Tremel, *J. Am. Chem. Soc.* **2015**, 137, 2285; b) M. Roming, C. Feldmann, Y. S. Avadhut, J. r. S. a. der Günne, *Chem. Mater.* **2008**, 20, 5787.

[34] W. Zhang, J. Yin, M. Sun, W. Wang, C. Chen, M. Altunkaya, A. H. Emwas, Y. Han, U. Schwingenschlogl, H. N. Alshareef, *Adv. Mater.* **2020**, 32, 2000732.

[35] W. Li, J. Yu, J. Wen, J. Liao, Z. Ye, B. Zhao, X. Li, H. Zhang, M. Liu, Z. Guo, *J. Mater. Chem. A* **2019**, 7, 16785.

[36] Z. Li, Y. Dong, J. Feng, T. Xu, H. Ren, C. Gao, Y. Li, M. Cheng, W. Wu, M. Wu, *ACS nano* **2019**, 13, 9227.

[37] a) N. Xiao, W. D. McCulloch, Y. Wu, *J. Am. Chem. Soc.* **2017**, 139, 9475; b) W. Zhang, Z. Wu, J. Zhang, G. Liu, N.-H. Yang, R.-S. Liu, W. K. Pang, W. Li, Z. Guo, *Nano Energy* **2018**, 53, 967.

[38] P. Liu, D. Mitlin, *Acc. Chem. Res.* **2020**, 53, 1161.

[39] a) Y. Hwa, J. H. Sung, B. Wang, C.-M. Park, H.-J. Sohn, *J. Mater. Chem.* **2012**, 22, 12767; b) A. Varzi, L. Mattarozzi, S. Cattarin, P. Guerriero, S. Passerini, *Adv. Energy Mater.* **2018**, 8, 1701706.

[40] D. Li, Y. Zhang, Q. Sun, S. Zhang, Z. Wang, Z. Liang, P. Si, L. Ci, *Energy Storage Mater.* **2019**, 23, 367.

[41] C. Li, X. Wang, W. Deng, C. Liu, J. Chen, R. Li, M. Xue, *ChemElectroChem* **2018**, 5, 3887.

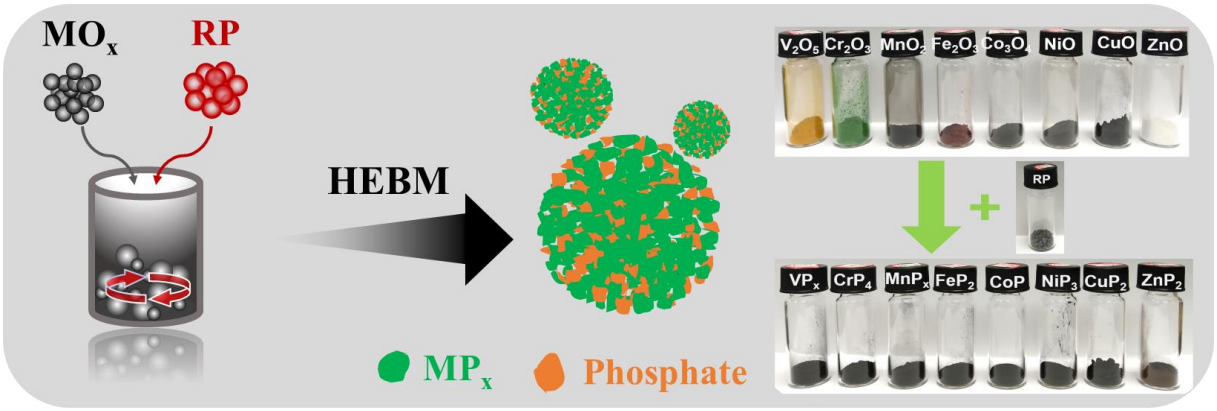


**Scheme 1.** Schematic illustration of the preparation of metal phosphide composites embedded with in situ-formed amorphous phosphates by one-step ball milling (left) and optical photos of raw materials and partial products (right).

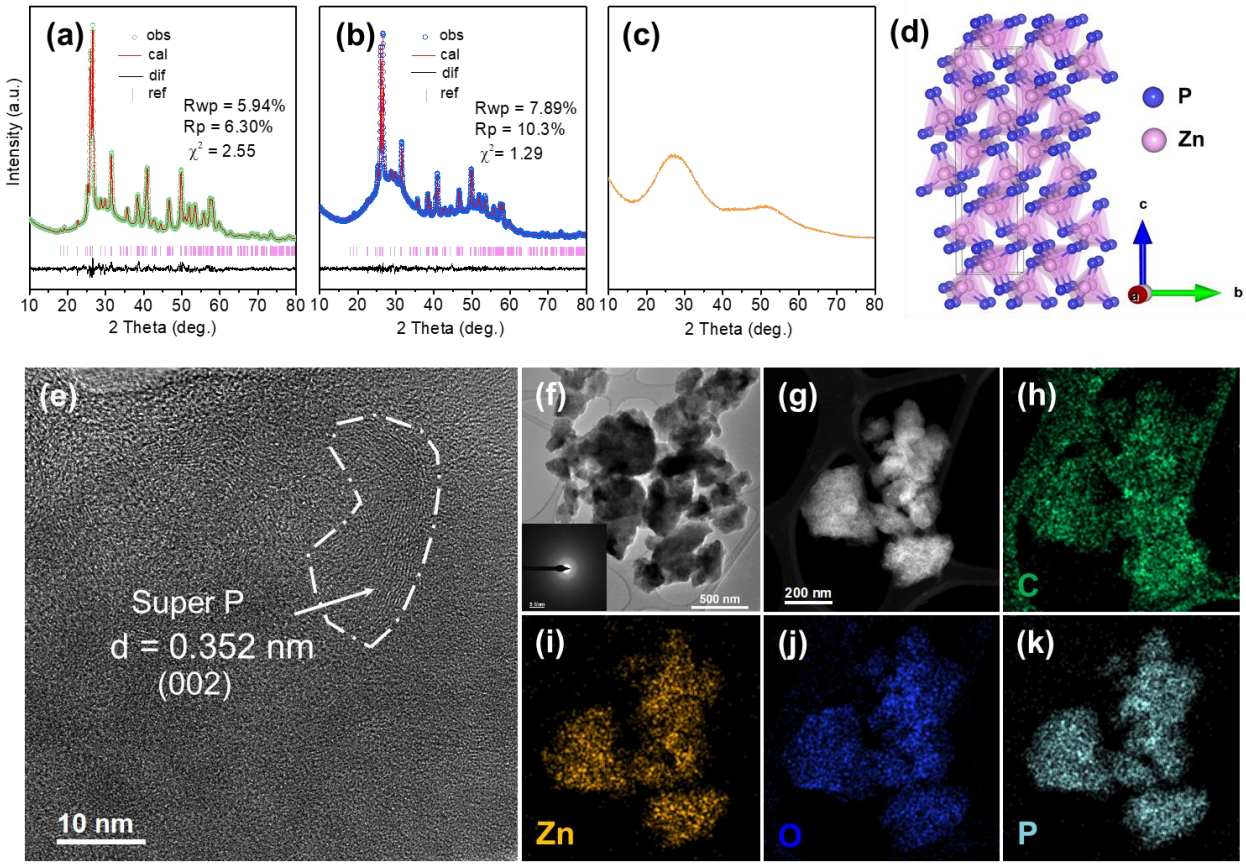


**Figure 1.** Structure and morphology characterizations. (a–c) XRD patterns with corresponding Rietveld refinement of ZnO@P(2:3), Zn@P(1:2)@C, and ZnO@P(1:2)@C. (d) Crystal structure of $ZnP_2$ with tetragonal phase and $P4_12_12$ space group. (e, f) HRTEM image, TEM image, and ED pattern (inset) of ZnO@P(1:2)@C. (g–k) HAADF–STEM image of ZnO@P(1:2)@C and the corresponding EDS elemental mappings of C, Zn, O, and P.

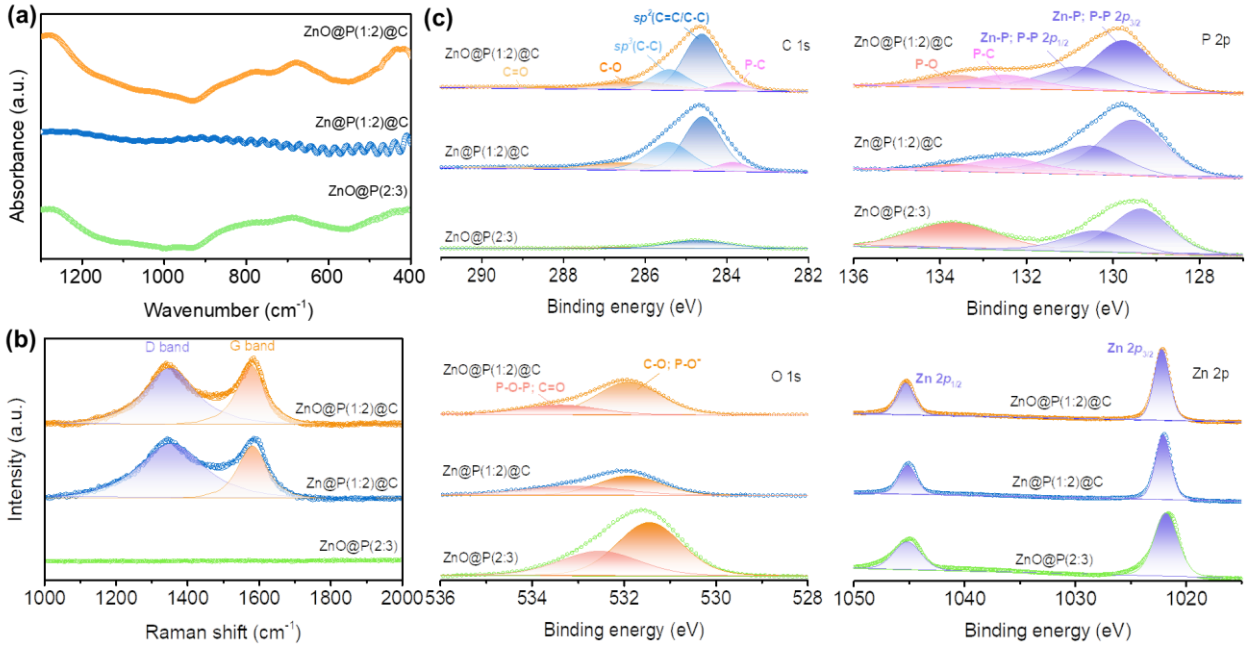


**Figure 2.** Chemical composition characterizations. (a) FTIR spectra and (b) Raman spectra of ZnO@P(1:2)@C, Zn@P(1:2)@C, and ZnO@P(2:3). (c) High-resolution XPS spectra of C1s, P2p, O1s, and Zn2p.

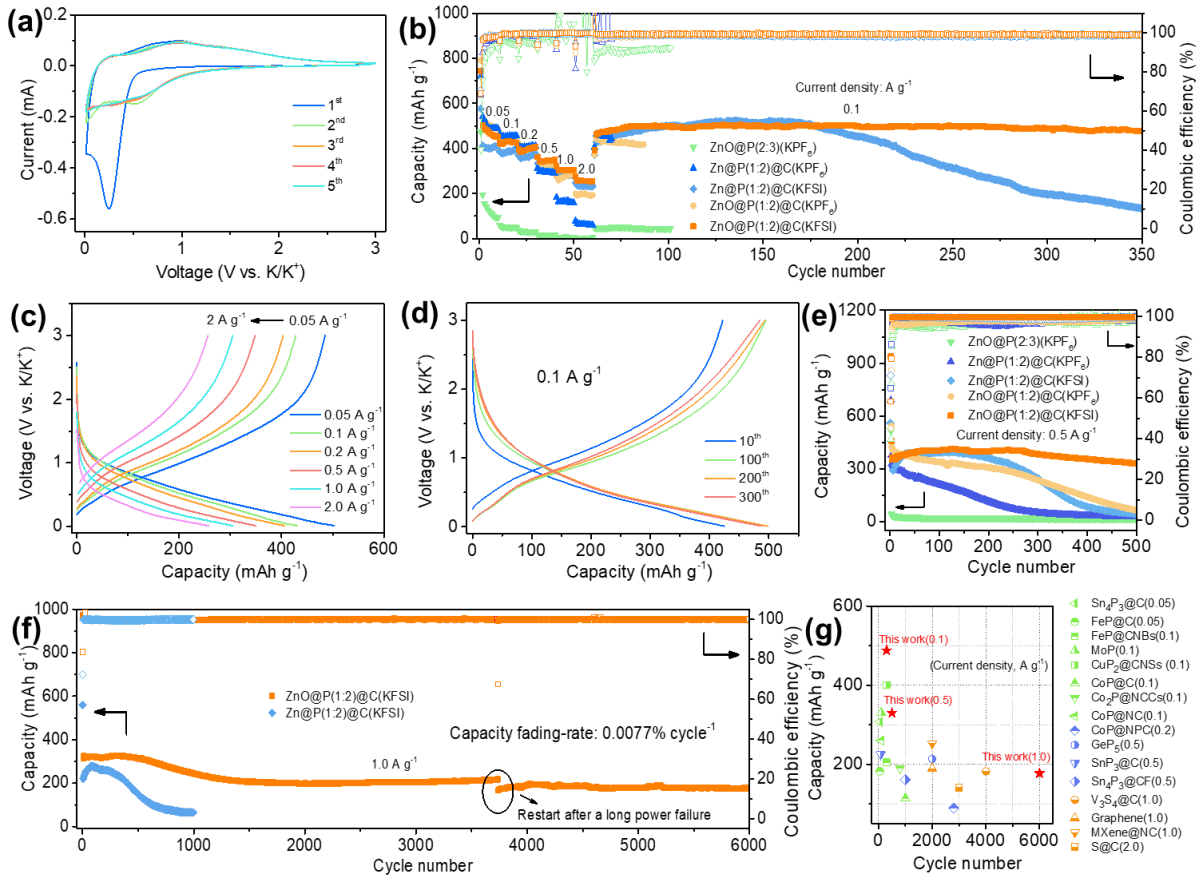


**Figure 3.** K-ion storage properties. (a) Initial five CV curves of ZnO@P(1:2)@C electrode at a scan rate of 0.05 mV $s^{-1}$ in the voltage range of 0.01–3.0 V versus $K/K^+$ in KFSI electrolyte. (b) Rate capabilities of ZnO@P(1:2)@C, Zn@P(1:2)@C, and ZnO@P(2:3) in $KPF_6$ and KFSI electrolytes. (c) Charge/discharge curves of ZnO@P(1:2)@C at current densities of 0.05–2.0 A $g^{-1}$ in KFSI electrolyte. (d) Charge/discharge curves of ZnO@P(1:2)@C at 10th, 100th, 200th, and 300th cycles at a current density of 0.1 A $g^{-1}$ in KFSI electrolyte. (e) Cycle performances of ZnO@P(1:2)@C, Zn@P(1:2)@C, and ZnO@P(2:3) at a current density of 0.5 A $g^{-1}$ in $KPF_6$ and KFSI electrolytes. (f) Long-term cycle performances of ZnO@P(1:2)@C and Zn@P(1:2)@C at 1.0 A $g^{-1}$ in KFSI electrolyte. (g) Comparison of cycle performances of ZnO@P(1:2)@C with reported metal phosphides and other advanced PIB anodes, including $Sn_4P_3$@C,[11b] FeP@C,[20d] FeP@CNBs,[14b] MoP,[20c] $CuP_2$@CNSs,[17a] CoP@C,[13d] $Co_2P$@NCCs,[13b] CoP@NC,[20e] CoP@NPC,[13c] $GeP_5$,[37b] $SnP_3$@C,[11a] $Sn_4P_3$@CF,[10d] $V_3S_4$@C,[15] Graphene,[4c] MXene@NC,[16c] and S@C[4d]; the numbers in brackets are the current densities (A $g^{-1}$), and the color code represents the current density range: green is less than or equal to 0.1 A $g^{-1}$, blue is 0.2–0.5 A $g^{-1}$, and orange is greater than or equal to 1.0 A $g^{-1}$.

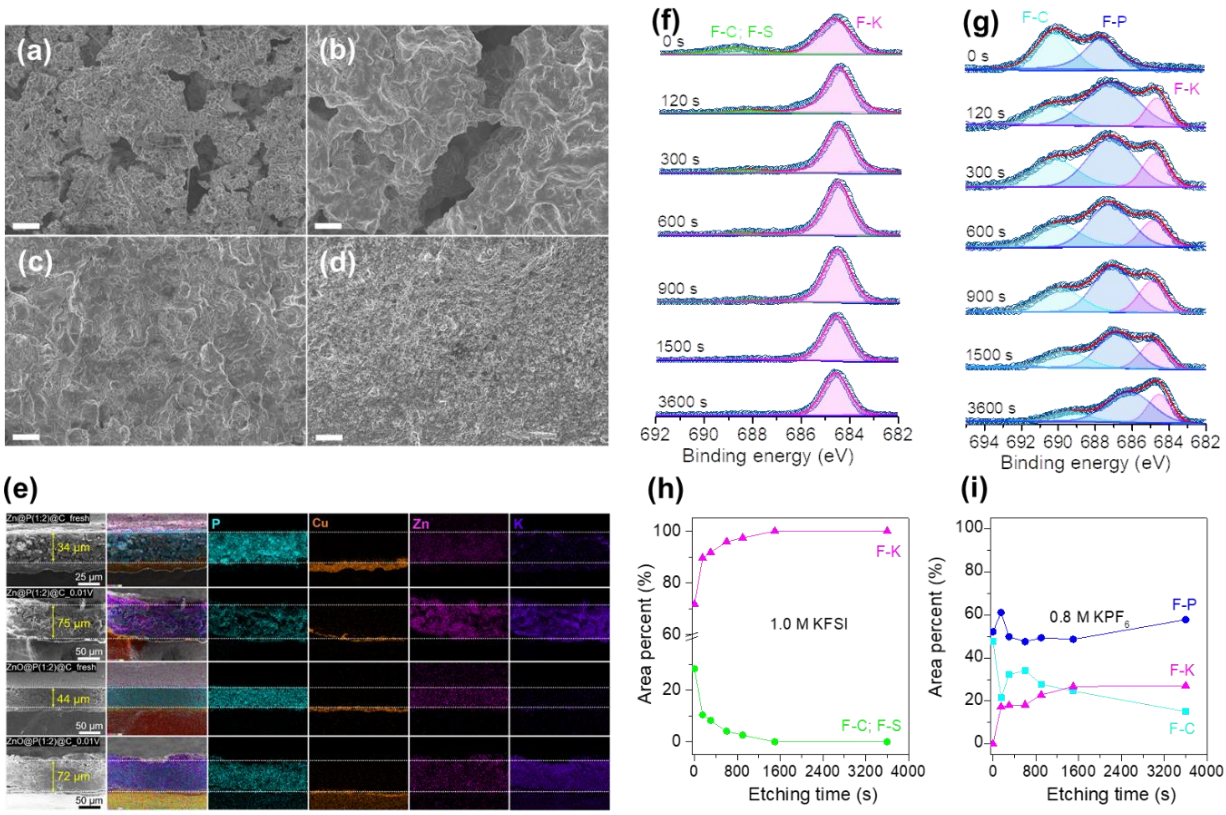


**Figure 4.** Characterization of electrode morphologies and SEI after cycling. SEM images of electrodes for (a) Zn@P(1:2)@C in $KPF_6$ electrolyte, (b) Zn@P(1:2)@C in KFSI electrolyte, (c) ZnO@P(1:2)@C in $KPF_6$ electrolyte, and (d) ZnO@P(1:2)@C in KFSI electrolyte after 500 cycles at 0.5 A $g^{-1}$, scale bars: 10 μm. (e) Cross-sectional SEM images and EDS elemental mappings of Zn@P(1:2)@C and ZnO@P(1:2)@C electrodes before and after discharging to 0.01 V with a current density of 0.05 A $g^{-1}$ in KFSI electrolyte. Etching XPS spectra of F 1s and corresponding area percentage of fitted peaks for ZnO@P(1:2)@C in (f, h) KFSI electrolyte and (g, i) $KPF_6$ electrolyte after 500 cycles at 0.5 A $g^{-1}$.

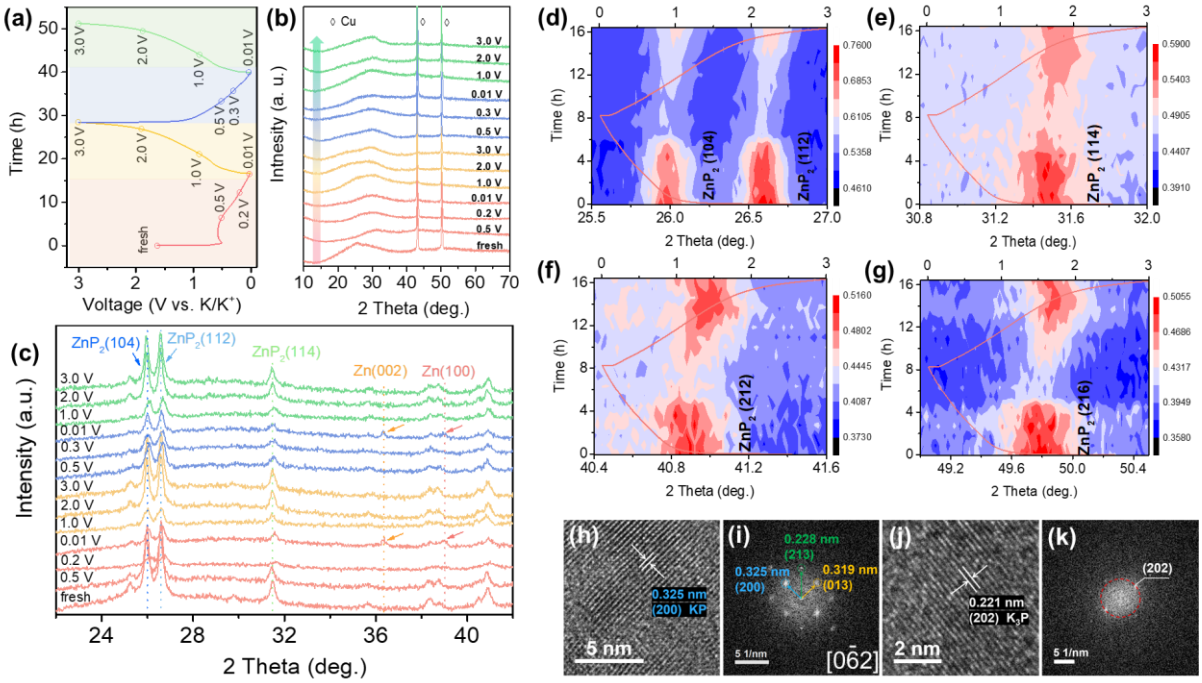


**Figure 5.** Mechanism analysis of potassiation and depotassiation reactions. (a) First two discharge/charge curves of ZnO@P(1:2)@C at 0.05 A $g^{-1}$ in KFSI electrolyte. Ex situ XRD patterns at different charge/discharge depths for (b) ZnO@P(1:2)@C electrodes and (c) Zn@P(1:2)@C electrodes in KFSI electrolyte. (d–g) Contour plots of in situ XRD of Zn@P(1:2)@C electrodes with overlayed voltage profiles shown for selected 2θ ranges. (h–k) HRTEM images and corresponding fast Fourier transformation patterns of Zn@P(1:2)@C electrode after discharging to 0.01 V.

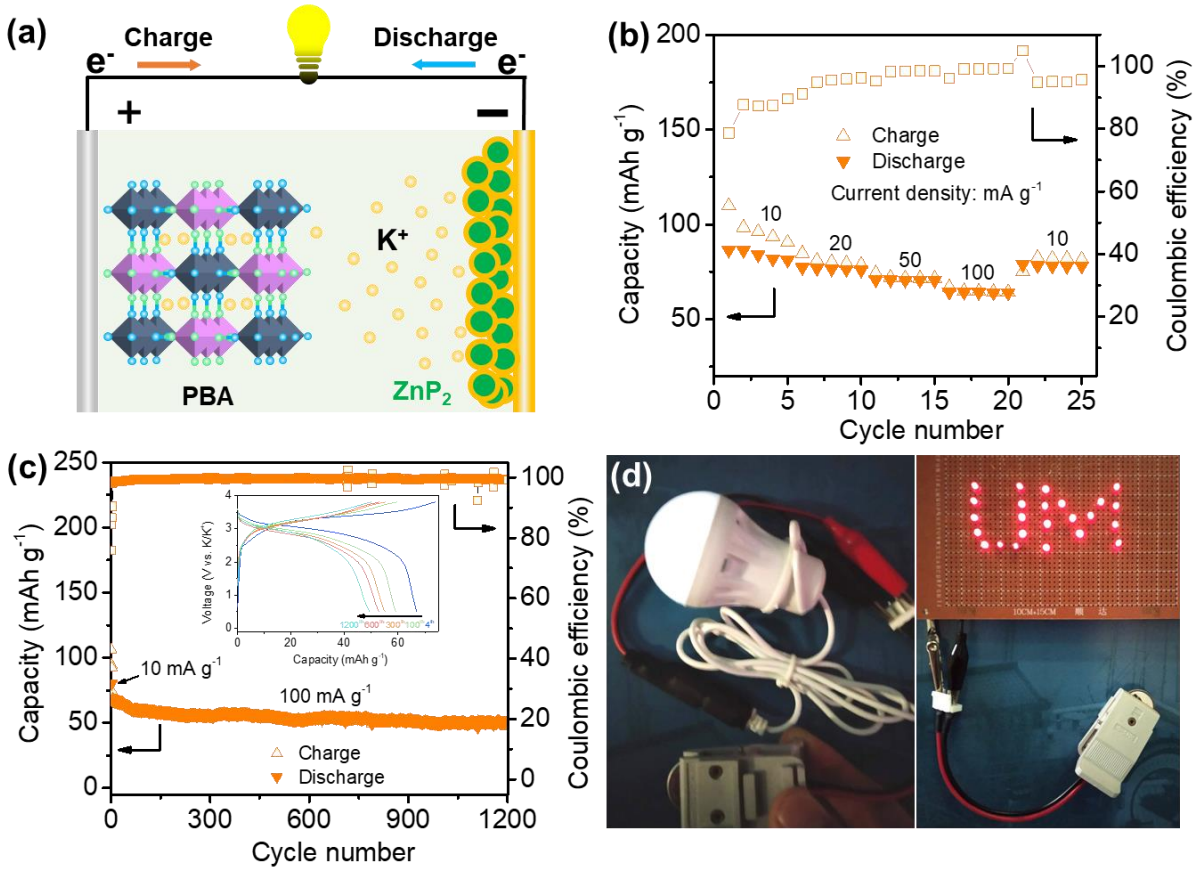


**Figure 6.** Full cell for K-ion storage. (a) Schematic of PBA//ZnO@P(1:2)@C. (b) Rate performance of full cell at different current densities. The inset in (b) shows the corresponding galvanostatic charge/discharge profiles of the full cell at different current densities. (c) Cycle performance of full cell at 100 mA $g^{-1}$. The inset in (c) shows the corresponding galvanostatic charge/discharge profiles at different cycles. (d) Optical images of full cell powering an energy saving lamp (1.5 W) and red LEDs.

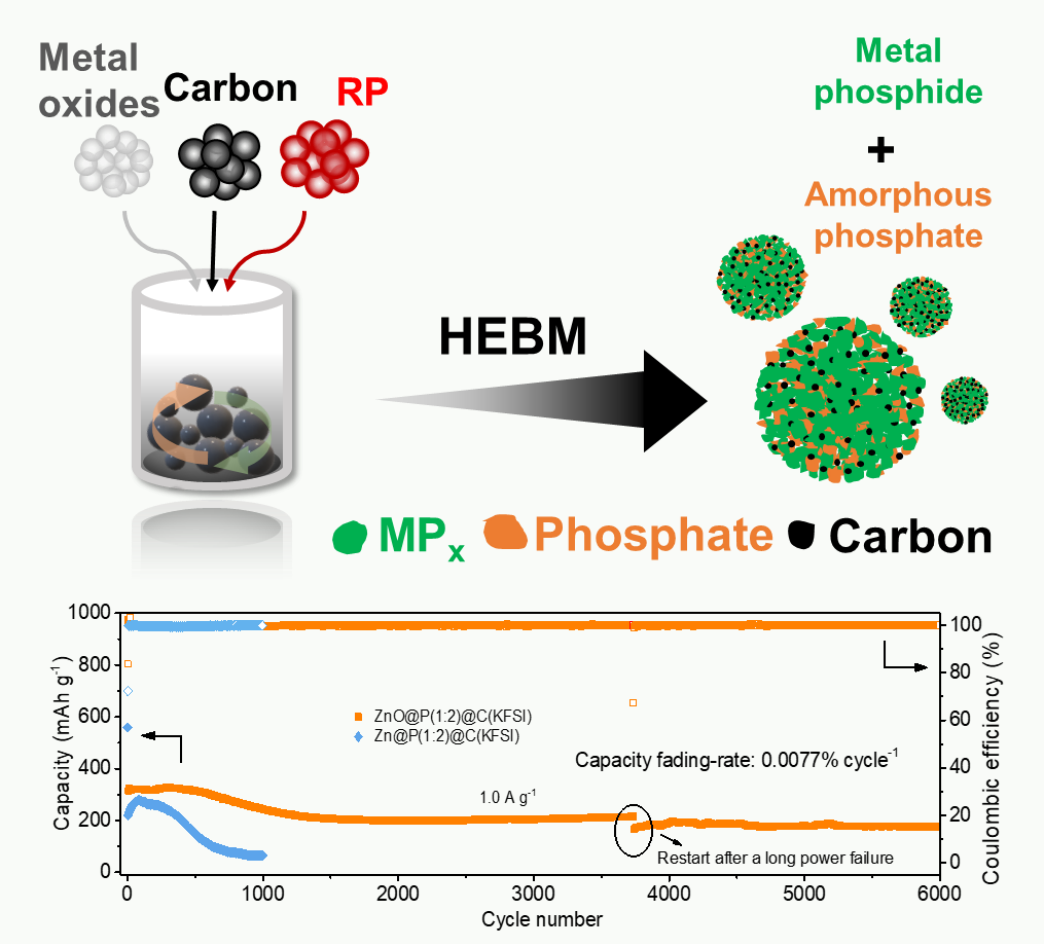


ToC

A universal strategy for preparing metal phosphides embedded with in situ-formed amorphous phosphates to function as buffer materials is proposed. The existence of amorphous phosphates can effectively reduce the volume expansion of metal phosphide electrodes and improves SEI and cycling stability when used as anodes for potassium-ion batteries in the KFSI-based electrolyte.